



**HAL**  
open science

## Microstructure and mechanical properties of high niobium containing TiAl alloys elaborated by spark plasma sintering

Houria Jabbar, Jean-Philippe Monchoux, Florent Houdellier, Mickaël Dollé, Frank-Peter Schimansky, Florian Pyczak, Marc Thomas, Alain Couret

### ► To cite this version:

Houria Jabbar, Jean-Philippe Monchoux, Florent Houdellier, Mickaël Dollé, Frank-Peter Schimansky, et al.. Microstructure and mechanical properties of high niobium containing TiAl alloys elaborated by spark plasma sintering. *Intermetallics*, 2010, 18 (12), pp.2312-2321. 10.1016/j.intermet.2010.07.024 . hal-01742044

**HAL Id: hal-01742044**

**<https://hal.science/hal-01742044>**

Submitted on 21 Jun 2019

**HAL** is a multi-disciplinary open access archive for the deposit and dissemination of scientific research documents, whether they are published or not. The documents may come from teaching and research institutions in France or abroad, or from public or private research centers.

L'archive ouverte pluridisciplinaire **HAL**, est destinée au dépôt et à la diffusion de documents scientifiques de niveau recherche, publiés ou non, émanant des établissements d'enseignement et de recherche français ou étrangers, des laboratoires publics ou privés.

***Final Draft***  
**of the original manuscript:**

Jabbar, H.; Monchoux, J.-P.; Houdelier, F.; Dolle, M.; Schimansky, F.-P.;  
Pyczak, F.; Thomas, M.; Couret, A.:

**Microstructure and mechanical properties of high niobium  
containing TiAl alloys elaborated by spark plasma sintering**

In: Intermetallics ( 2010) Elsevier

DOI: 10.1016/j.intermet.2010.07.024

# Microstructure and mechanical properties of high niobium containing TiAl alloys elaborated by Spark Plasma Sintering

Houria Jabbar<sup>1,2</sup>, Jean-Philippe Monchoux<sup>1,2</sup>, Florent Houdellier<sup>1,2</sup>, Mickael Dollé<sup>1,2</sup>,  
Frank-Peter Schimansky<sup>3</sup>, Florian Pyczak<sup>3</sup>, Marc Thomas<sup>4</sup> and Alain Couret<sup>1,2,\*</sup>

1 : CNRS ; CEMES (Centre d'Elaboration de Matériaux et d'Etudes Structurales) ; BP 94347,  
29 rue J. Marvig, F-31055 Toulouse, France

2 : Université de Toulouse ; UPS ; F-31055 Toulouse, France

3 : Institute for Materials Reserch, GKSS Research Centre, D-21502 Gesthacht, Germany

4 : DMMP/ONERA, 29 Avenue de le Division Leclerc, BP 72, 92322 Châtillon Cedex, France

\* corresponding author

## Abstract

Spark Plasma Sintering (SPS) is used to process TNB alloys. Pre-alloyed powders (Ti-46Al-9Nb) were sintered between 975°C and 1300°C under 100MPa. The microstructures of the products are determined by X-ray diffraction and by scanning and transmission electron microscopy. Their mechanical properties are evaluated by tensile tests performed at room temperature and creep experiments at 700°C under 300 MPa stress.

Depending on the sintering temperature, two-phased, duplex and lamellar microstructures have been obtained. A quasi- $\alpha_2$  phase has been observed, which is in fact an  $\alpha_2$  phase in which Nb atoms have substituted Ti atoms. The TNB alloys consolidated by SPS are stronger than the alloys previously elaborated by SPS using Ti-47Al-2Cr-2Nb and Ti-44Al-2Cr-2Nb-1B powders but they exhibit a lower ductility. Moreover, some specimens broke prematurely due to Fe inclusions.

## 1. Introduction

Since the pioneering works of Chen et al. [1] and Huang et al. [2], it is well known that high niobium TiAl alloys (called TNB alloys) exhibit significantly improved mechanical strength from room temperature to 800°C, with respect to conventional  $\gamma$ -TiAl alloys. To our knowledge, the best compromise of room temperature properties for TNB alloys combine an exceptional ductility of 2.5% and a yield stress higher than 1GPa [3]. Liu et al. [4] and Zhang et al. [5] have shown that this mechanical strength is enhanced by a reduced aluminium content (~ 45 at. %) for both lamellar and near- $\gamma$  alloys. The high strength of TNB alloys was interpreted to result from solid solution hardening via Nb atoms [4,5] and/or by a Hall-Petch effect, due to a refinement of the microstructure by Nb addition [6-8]. Furthermore, the

strength of TNB alloys can also be increased by hot working. In the case of a number of extruded Ti-45Al-(5-10Nb)-C alloys deformed at room temperature, a good repeatability was obtained in terms of yield stress [9]. However, high scattering in work hardening and tensile ductility were encountered and explained by microstructural heterogeneities. The addition of boron is also beneficial to refine the microstructure and improve the ductility, only for the case of duplex microstructures [10]. Concerning the creep properties, lamellar microstructures exhibit the best creep resistance, and carbon additions can further improve the creep behaviour [7].

In this context, powder metallurgy appears to be a route to homogenize the microstructure. This was investigated in detail for Ti-46Al-9Nb cross-rolled sheet material [11-13]. The near- $\gamma$  microstructures exhibit very high strength and creep resistance but limited ductility at low temperatures. The large amount of Nb in the latter alloy is found to enhance the creep resistance by reducing the diffusivity [11]. The Spark Plasma Sintering (SPS) technique in which the powder is sintered through the simultaneous application of a pulsed direct current of high intensity and uniaxial pressure (a recent review on this technique is given in [14]), has been successfully used to produce TiAl alloys with different microstructures. On the one hand, nanostructured materials with high yield stress at room temperature were obtained by sintering [15-17]. However, such materials are characterized by a lack of tensile ductility and a low creep resistance at high temperature. On the other hand, the SPS processing of pre-alloyed GE powder (Ti-47Al-2Cr-2Nb) and boron-containing GE powder (Ti-44Al-2Cr-2Nb-1B) has produced two-phased and duplex microstructures, respectively which have shown satisfactory room temperature ductility (about 2%) and good tensile strength, combined with very good reproducibility of microstructure and mechanical properties for different specimens [18,19]. On the other hand, only limited creep resistance was obtained. The aim of the present work is thus to investigate the capability of the SPS route to produce TNB TiAl alloys with balanced mechanical properties for high temperature structural applications. Baring in mind previous studies of cast and forged TNB alloys, a major goal was to improve creep resistance after SPS processing. It should be underlined that Ti-45Al-8.5Nb-(W,B,Y) powders were recently sintered by SPS [20-22]. In such alloys, near- $\gamma$ , duplex and fully lamellar microstructures were achieved depending on the sintering conditions, combined with high mechanical strength in compression over the temperature range 1100°C to 1250°C. Lu et al. [22] have obtained high strength combined with good ductility (1.15%) in tension for TNB alloys at room temperature.

## 2. Experimental

A Ti-46Al-9Nb alloy was atomized by the cold crucible PIGA technique (Plasma melting Induction Guiding gas Atomization) developed at GKSS Research Centre, (Geesthacht, Germany) especially for titanium alloys [23]. Powder particles with a size smaller than 180  $\mu\text{m}$  were used for SPS processing. When compacted by SPS we will term this alloy from now on TNB9-SPS. The majority phase observed in the atomised powder is  $\alpha_2$ , which indicates that the powder is out of equilibrium due to the high cooling rate of  $10^3$ - $10^4$  K/s experienced during atomization [24]. A significant amount of  $\beta$  phase was also detected.

For the SPS processing, the same procedure for TiAl alloys as described in Ref [19] was followed. For each experiment, the temperature rise was initially 100 K/min and then reduced to 25 K/min during the last three minutes, in order to prevent temperature overshooting. Cylindrical samples with typical diameters of 8mm and 36 mm (from now on termed  $\varnothing 8$  and  $\varnothing 36$  samples) were sintered using a constant pressure of 100 MPa and a 2 min holding time at the temperature plateau. For these experiments, the measured temperature corresponds to the external temperature at the surface of the graphite die. In previous work on GE TiAl powders [19], the temperature in the sample core was found to be 25 K and 150 K higher for the  $\varnothing 8$  and  $\varnothing 36$  samples, respectively. During the present experiments, a graphite felt was wrapped around the die to limit the heat loss by radiation, thus reducing the difference between external and sample temperature to 100 K for  $\varnothing 36$  samples. The sample temperature  $T_s$  and the SPS (external) temperature  $T_{\text{SPS}}$  will be given in the following.

Phase identification was carried out by means of X-ray diffraction analysis and transmission electron microscopy (TEM) studies in diffraction modes. The microstructures were studied in a scanning electron microscope (SEM) using back scattered electron imaging (BSE) and in TEM. TEM foils were prepared by standard jet polishing using the A3 electrolyte commercialised by Struers at  $-10^\circ\text{C}$  with a current of 500 mA and a voltage of 90 V. TEM investigations were performed on a JEOL 2010 operating at 200 keV and a FEI CM30 equipped with electronic precession (Nanomegas device) operating at 300 keV. CBED experiments were performed at 200 KeV in the FEI CM30. Three test specimens, suitable for tensile tests at room temperature (strain rate  $10^{-4}\text{s}^{-1}$ ) and creep experiments at  $700^\circ\text{C}$  and 300 MPa (under constant stress), were machined from each  $\varnothing 36$  SPS processed billet.

### 3. Evolution of the microstructure with the temperature

The microstructures and the X-ray diffractograms of Ø8 samples sintered at various temperatures are depicted in Fig. 1.

#### 3.1. Experiment with $T_s = 975^\circ\text{C}$

In a preliminary study some experiments at very low sintering temperatures were carried out in order to gain a better understanding of the overall SPS process. The SEM BSE micrograph of a Ø8 sample sintered at  $T_s = 975^\circ\text{C}$  ( $T_{\text{SPS}} = 950^\circ\text{C}$ ) is shown in Fig. 1b. Under these conditions, compaction is far from complete, and the powder particles are clearly delimited by voids. During this low-temperature SPS annealing, the  $\alpha_2$  phase is nearly fully transformed into the  $\gamma$  phase, as illustrated by the XRD pattern that shows almost no presence of the  $\alpha_2$  phase (Fig. 1a). It thus appears that, when the sintering starts, the powder has reached equilibrium since the  $\alpha \rightarrow \gamma$  transformation is completed.

In Fig. 1b, several particles with different sizes can be observed, all of them exhibiting a dendritic structure. EDX analysis was carried out on different particles to study the Ti, Al and Nb distributions in the dendritic structure: Nb concentrates in the dendrite cores, Al segregates to the interdendritic channels and Ti seems to be relatively homogeneously distributed. Table 1 gives the difference between the average composition of dendrite cores and interdendritic channels. This dendritic morphology of the powder and the measured chemical composition are very similar to previous results described in Refs [20,25]. As illustrated in Fig. 1b, the dendritic structure is more pronounced and less fragmented in some particles and there is a tendency that large particles show an especially well developed dendritic structure. The fact that the dendritic morphology is strongly pronounced indicates significant difference in Al and Nb contents.

#### 3.2. Experiments at $T_s = 1250^\circ\text{C}$ and $T_s = 1275^\circ\text{C}$

At  $T_s = 1250^\circ\text{C}$  ( $T_{\text{SPS}} = 1225^\circ\text{C}$ ) and  $T_s = 1275^\circ\text{C}$  ( $T_{\text{SPS}} = 1250^\circ\text{C}$ ), the diffractograms (Fig. 1a) show that the samples are composed of two phases, the  $\gamma$ -phase and a hexagonal phase.

At  $T_s = 1250^\circ\text{C}$  (Fig. 1c), the microstructure as observed by SEM has a two-phased character. The dark grains consist of  $\gamma$  phase whereas areas with bright contrast appear as laths and grains. Irrespective of their outer shape both exhibit a tweed contrast (see examples in Fig. 2) under certain diffraction conditions in TEM. In section 4, it will be shown that this

phase is not the classical  $\alpha_2$  phase but a quasi- $\alpha_2$  phase. It will be shown in section 5.1, that the  $\gamma$  grains also contain precipitates of the B2 phase.

At  $T_s = 1275^\circ\text{C}$  (Fig. 1d) lamellar colonies are observed together with  $\gamma$  grains and we will term this microstructure as duplex in the following. A smaller volume fraction of laths is present than observed at  $T_s = 1250^\circ\text{C}$ , i.e. the volume fraction of laths is decreased as the temperature is increased.

These two-phased and duplex microstructures will be analysed in details in the following sections. Moreover, some mechanical properties are presented in section 6 of this paper.

### 3.3. Experiments at $T_s \geq 1300^\circ\text{C}$

At  $T_s = 1300^\circ\text{C}$  ( $T_{\text{SPS}} = 1275^\circ\text{C}$  - Fig. 1e), a lamellar microstructure is observed, indicating that the temperature lies above the  $\alpha$  transus during SPS. A large scatter in the size of the lamellar colonies is observed, and it appears that rapid grain coarsening has occurred. Further investigations on this coarse lamellar microstructure were not carried out, since it does not appear promising for structural applications. For instance, fully lamellar microstructures in TNB powders processed using combustion synthesis followed by compaction have shown poor ductility and a limited strength at room temperature in recent work [26].

## 4. The quasi- $\alpha_2$ phase with a tweed contrast

Under TEM observation the grains and laths of the quasi- $\alpha_2$  phase exhibit a tweed contrast under some diffraction conditions, which reveals that this phase is not the usual  $\alpha_2$  phase (Fig. 2). Some bright and dark zones as well as some contrast modulations can be observed. Several electron diffraction techniques have been used to determine the corresponding structure. A first indication, given by electronic precession [27] experiments, was that this phase has a hexagonal structure. However, as shown below, analyses in electronic precession diffraction and Convergent Beam Electron Diffraction (CBED) modes have demonstrated that the crystallography of this tweed structure does not fit with the  $\text{DO}_{19}$  structure of the  $\alpha_2$  phase.

Electronic precession patterns taken from four different zone axes revealed a space group which is different from the  $\alpha_2$  space group  $\text{P6}/\text{mmc}$ . For instance, in figure 3, experimental patterns are compared with a calculated pattern (Fig. 3b) for the case of the  $[0001]$  zone axis of the  $\text{DO}_{19}$  structure. One experimental diffraction spot in the FOLZ (marked by an arrow) is

clearly visible (Fig. 3a) whereas the corresponding reflection is forbidden for the DO<sub>19</sub> structure as shown in the simulated pattern.

Fig. 4 a & b show CBED patterns, which were recorded under an illumination condition away from a low indexed zone axis at various locations within a tweed grain with a 1nm sized probe. Some changes on the HOLZ lines are discernable. On the pattern shown in Fig. 4a, the excess line (visible in the enlargement) has a clear contrast which is indicative of a long range ordered structure. On the contrary, the same excess line in the pattern Fig. 4b is fuzzy due to some secondary maxima. This broadening of HOLZ lines indicates a variation of the lattice parameter along the electron pathway [28], which can be interpreted in terms of a chemical order variation. Finally, the CBED pattern recorded along the [0001] zone axis (Fig. 4c) exhibits a symmetry loss with respect to the 6 order symmetry of a hexagonal structure, as illustrated by the angles and the distances between the different spots.

As a conclusion, it is proposed that this quasi- $\alpha_2$  phase is an  $\alpha_2$  phase in which the substitution of Ti atoms by Nb atoms led to a decay in the long range order and the loss of the hexagonal crystallographic symmetry, which could explain the diffraction patterns and the tweed contrast. Further work is in progress to determine the space group of this quasi- $\alpha_2$  phase.

In a Ti-(40-44)Al-Nb alloy Appel et al. [29] also observed laths with periodic variations in the image contrast. As shown by their high resolution electron microscopy (HREM) investigations (see Fig. 2 of [29]), these laths are formed by regions with different crystalline structures contrary to the TNB9-SPS alloy for which our HREM pictures evidence an equal crystallographic structure (Fig. 5).

## 5. SPS microstructures

### 5.1. Two-phased microstructure containing B2 precipitates

Fig. 6 shows SEM and TEM micrographs at various magnifications of the two-phased microstructure. Two major phases can be identified in the SEM micrographs (see for instance Fig. 6b): the  $\gamma$  phase with a grey-dark contrast which forms the matrix and the quasi- $\alpha_2$  phase with a brighter contrast. Additionally dispersed particles with bright contrast (probably B2) are discernible. Some quasi- $\alpha_2$  grains and laths are indicated by arrows and some B2 precipitates are encircled. Note that the volume fraction of the B2 phase is quite low, i.e. below the detectable level in the XRD pattern in Fig. 1a. This justifies terming this microstructure as two-phased. EDX point analyses of the different phases are given in Table

2. The BSE contrast between the  $\gamma$  and the quasi- $\alpha_2$  results from the difference in Ti/Al ratio, while the brighter contrast of the B2 precipitates results from both a high Ti/Al ratio in combination with a higher Nb content.

The quasi- $\alpha_2$  phase appears as a lath morphology with a high aspect ratio as well as in the form of intergranular grains located at  $\gamma$  grain boundaries (Fig. 6b). This micrograph also indicates that rings of intergranular quasi- $\alpha_2$  grains could be present at the periphery of the former powder particles (black and white arrows in Fig. 6a). This precipitation may be promoted by oxide layers present at former particle surfaces.

Different types of  $\gamma$  matrix grains can be distinguished: some large grains (A) containing laths with different orientations and numerous small grains (B) without laths which are generally bordered by intergranular quasi- $\alpha_2$  grains (the dashed rectangles indicate areas containing grains of B type). The large  $\gamma$  grains can extend over several dendrites (one example is shown in Fig. 6a where interdendritic regions are clearly visible), and can contain laths with different orientations. Fig. 6c shows a TEM micrograph of such grains. Using coupled diffraction and stereographic analyses, the elongated direction of the laths has been determined to be parallel to the  $\{111\}$  planes of the  $\gamma$  grains. It is also discernable that these laths containing  $\gamma$  grains include deformation dislocations, which probably resulted from the sintering process. The average size of the small  $\gamma$  grains present in zones marked (B) is in the order of 2-5  $\mu\text{m}$  and many quasi- $\alpha_2$  grains (represented as grey zones in the scheme of Fig. 6d) can be seen in these areas. On this TEM micrograph (Fig. 6d), such small  $\gamma$  grains are clearly imaged without contrast variations in their interior because they are free of dislocations. Hence, it is suggested that these fine grains result from recrystallisation processes.

## 5.2. Duplex microstructures

Fig. 7 (TEM) illustrates the duplex microstructure, which is composed of several types of grains:

- Some lamellar grains with sizes in the range of 5 to 15  $\mu\text{m}$ . Two examples of such lamellar colonies can be found in Figs 7a & c, both are surrounded by recrystallised  $\gamma$  grains. It is interesting to note that the two lamellar colonies shown in Figs 7a & c are formed by two different types of lamellar transformations which are known from literature [30]. In the case of Fig. 7a & b, the lamellar microstructure results from the usual high temperature transformation  $\alpha \rightarrow \alpha + \gamma \rightarrow \alpha_2 + \gamma$ . In the case of Fig. 7c &

d, the  $\alpha_2$  lamellae exhibit some antiphase boundaries which are crossed by thin  $\gamma$  lamellae, as can be seen in the dark field image of the enlargement of Fig. 7d. This indicates that the fine  $\gamma$  lamellae precipitated subsequent to the ordering transformation  $\alpha \rightarrow \alpha_2$  at a lower temperature.

- Some recrystallised  $\gamma$  grains, with similar appearance to those observed in the two-phased microstructure but with a larger average size (5 to 10  $\mu\text{m}$ ). Also intergranular quasi- $\alpha_2$  precipitates are also present. Their size is larger than at lower temperature as expected.
- A few  $\gamma$  grains containing laths (Fig. 7e), similar to those observed in the two-phased microstructure. Here again, their size increases with increasing SPS sintering temperature.

## 6. Mechanical properties

For mechanical tests, six  $\text{Ø}36$  powder compacts with homogeneous microstructures were successfully sintered in the  $T_S$  range between  $1240^\circ\text{C}$  and  $1290^\circ\text{C}$ . It was very difficult to find the plateau temperature allowing the formation of a duplex microstructure similar to that obtained for the  $\text{Ø}8$  samples. In fact a series of 6 sinter treatments was performed in order to obtain the two duplex specimens. The two-phased microstructure was obtained at  $T_S = 1240^\circ\text{C}$ ,  $T_S = 1250^\circ\text{C}$  and  $T_S = 1260^\circ\text{C}$ . At  $T_S = 1275^\circ\text{C}$ , the core of the billet exhibits a duplex microstructure whereas a two-phased microstructure is observed at the outer surface. At  $T_S = 1280^\circ\text{C}$  and  $T_S = 1290^\circ\text{C}$ , a homogeneous duplex microstructure is observed. The difficulties encountered in attaining the desired final microstructure are attributed to the extreme sensitivity of the phase transformations on the sintering temperature under and local chemical composition under such processing conditions. This is exemplified by the simultaneous presence in the same specimen of lamellar colonies formed by a transformation mechanism typical for slow cooling rates and others colonies formed by a transformation mechanism typical for fast cooling rates, as shown in Figs. 7a & c.

Tensile properties at room temperature are illustrated in Fig. 8 and summarized in Table 3 with the entire set of data displayed. The curves present similar shapes, with a low work hardening. Two specimens sintered at  $T_S=1240^\circ\text{C}$  and  $T_S=1260^\circ\text{C}$  failed immediately beyond the yield point. One specimen sintered at  $T_S=1250^\circ\text{C}$  exhibits rupture at a low tensile elongation of 0.15% associated with a high UTS of 882 MPa. Four specimens ( $T_S=1250^\circ\text{C}$ ,  $T_S=1260^\circ\text{C}$ ,  $T_S=1280^\circ\text{C}$  and  $T_S=1290^\circ\text{C}$ ) show more promising properties with elongations of

0.88%, 0.78%, 0.56% and 0.44%, respectively and a strength levels ranging between 750 MPa and 900 MPa. For comparison, the tensile curve obtained for a HIPed specimen made from the same powder is also shown. With respect to SPS alloys made with GE powders, one can see an increase in YS and UTS but a strong decrease in tensile ductility [19].

The fracture surfaces of the broken specimens were analysed by SEM. Fig. 9 presents the cross section of one specimen that failed prematurely ( $T_s=1260^\circ\text{C}$ ), and shows that the crack initiation site coincides with an inclusion containing a high amount of Fe, as indicated by the EDS analysis in Fig. 9b (Table 4 - point 3). Similar Fe inclusions were detected in other tensile TNB9-SPS samples, however for these samples there was no clear correlation between these inclusions and the initiation of the crack. No Fe inclusions were found at the fracture surface of the as-HIPed tensile specimen. Following these results, the chemical composition of the initial powder was determined and a Fe content of about 0.02wt% was detected. A low amount of Fe was present as a impurity in the titanium sponge used to fabricate the initial ingot.

Creep curves at  $700^\circ\text{C}$  and 300 MPa for the two-phased microstructure are shown in Fig. 10, with the corresponding minimum creep rates given in Table 5. As for the tensile tests, the creep resistance is also strongly dependent on sintering temperature. However, it should be noted that two specimens showed minimum creep rates of 5 to 6.  $10^{-8} \text{ s}^{-1}$ , which is much lower than those obtained for GE-SPS alloys with similar microstructures [19].

## 7. Discussion

During SPS heating of the TNB powder, the  $\alpha_2$  phase transforms into  $\gamma$  phase with the retention of the dendritic morphology at a temperature lower than  $975^\circ\text{C}$ , thus prior to the onset of sintering. For  $\varnothing 8$  samples, the sintering is completed at  $T_s = 1200^\circ\text{C}$  and the  $\alpha$  transus is overcome between  $T_s = 1275^\circ\text{C}$  and  $T_s = 1300^\circ\text{C}$ . The minimum temperature required for fully compact TNB material is higher than that for Ti-47Al-2Cr-2Nb and Ti-44Al-2Cr-2Nb-1B powders. This is presumably due to higher mechanical strength of the TNB powder. By slow heating steps coupled with metallographic examinations, the  $\alpha$  transus temperatures of Ti-44Al-8Nb and Ti-45Al-7.5 Nb alloys were determined to be slightly below  $1280^\circ\text{C}$  [9] and  $1290^\circ\text{C}$  [31], respectively, whereas thermodynamic calculations give higher values ( $\sim 1320^\circ\text{C}$ ) [31,32]. The  $\gamma \rightarrow \alpha$  transformation during SPS experiments occurs over the same temperature range as for specimens under near equilibrium conditions.

The pseudo-binary Ti-Al phase diagrams for 8 and 10 at.% Nb given in Ref. [25] will thus be used to interpret the present results. Consistently with this diagram, a coarse lamellar grain structure is obtained for sintering temperatures above 1275 °C. As a matter of fact, the Al-content of the present TNB9-SPS alloy is too high and the Nb-content too low to facilitate a solidification through the  $\beta$  phase field, which is helpful in reducing the grain size. In the range from  $T_s = 1225^\circ\text{C}$  to  $T_s = 1275^\circ\text{C}$ , the microstructures are a mixture of  $\gamma$  grains and of quasi- $\alpha_2$  or lamellar areas. The latter are both transformed from high temperature  $\alpha$  phase. The higher the sintering temperature, the larger the volume fraction of these transformed former  $\alpha$  areas, in agreement with the phase diagram. As for the SPS material produced from GE powders [19], the duplex microstructure which requires the formation of  $\alpha$  grains is observed at sintering temperatures just below the  $\alpha$  transus. In the present study using TNB powder, control of the microstructure of  $\varnothing 36$  samples has been found to be a critical issue, in particular for obtaining the duplex microstructure. This is contrary to our previous experience for GE [19] and G4 (Ti-47Al-1Re-1W-0.2Si) [33] powders. Similar to our experience with GE and G4 powders, Lu et al. [22] did not encounter such difficulties using a Ti-45Al-8.5Nb-0.2W-0.2B-0.1Y powder since they were able to produce through sintering two-phased, duplex and lamellar microstructures by increasing sintering temperatures. In comparison to the current study the Ti-45Al-8.5Nb-(W,B,Y) SPS alloys presented in Ref. [20] exhibit more pronounced  $\beta$  and  $\alpha_2$  precipitates in the near  $\gamma$  and lamellar microstructures. In particular, the  $\beta$  segregation and/or boron for the latter seemed to limit the grain growth and thus plays a prominent role for retaining a fine microstructure. It could be interesting to perform TEM investigations on the TNB alloys sintered by SPS during these various studies [20-22] to check the presence of the quasi- $\alpha_2$  phase. Anyway, it appears that many differences exist for the TNB alloys sintered by SPS in this study compared to other SPS processed material presented in the literature. This can probably be explained by differences in the local chemical composition and the microstructure of the initial powders.

Concerning the tensile behaviour, the specimens can be classified into three groups (named GI to GIII in Table 3). The first group corresponds to those two samples that failed prematurely. This effect is probably due to Fe inclusions and so, we believe that these specimens do not exhibit the true intrinsic mechanical properties of TNB9-SPS alloys. Thus, it should be underlined that the quality of the powder must be very carefully controlled. The differences in yield stress (YS) and ultimate tensile strength (UTS) values distinguish the remaining samples into two groups: (GII (low YS and UTS):  $T_s = 1250^\circ\text{C}$  and  $T_s = 1290^\circ\text{C}$

and GIII (high YS and UTS):  $T_S = 1250^\circ\text{C}$ ,  $T_S = 1260^\circ\text{C}$  and  $T_S = 1280^\circ\text{C}$ . Note that all the stress-strain curves of these two groups show similar behaviour with low strain hardening leading to similar tensile ductilities of nearly 1% (except for the  $T_S = 1250^\circ\text{C}$  sample). However, it is surprising that: i) the group of samples cannot be distinguished from each other by the sintering temperature, ii) no difference in the mechanical behaviour is found between two-phased and duplex microstructures. iii) specimens of GII with lower YS than those of GIII exhibit a similar plastic deformation behaviour leading to lower UTS and similar tensile ductility. In other words, tensile ductility seems to be rather limited by a maximum strain than by the maximum stress level. For instance, Picca and coworkers [34] have proposed that rupture of TiAl alloys results from local stress concentrations due to locking of twin dislocations at lamellar interfaces or grain boundaries. In the present case, the large  $\gamma$  grains containing quasi- $\alpha_2$  laths, such as those shown in Fig. 4a, could concentrate many dislocations pile-ups, thus leading to a very high level of internal stress. As a result of better microstructural control, Lu et al. [22] have obtained better mechanical properties than obtained in this study, in particular a UTS of 1024 MPa and a plastic elongation to rupture of 1.16 % for the duplex microstructure.

It is worth noting that the creep properties of the TNB9-SPS alloys also present no clear dependence between the minimum creep rate and the sintering temperature. Even different samples sintered at the same temperature ( $T_S = 1250^\circ\text{C}$ ) exhibit different minimum creep rates. In comparison with current cast and forged TNB alloys with lamellar microstructures, TNB9-SPS alloys offer a lower creep resistance, which results probably from the possibility to the dislocations to move in the  $\gamma$  matrix without interaction with lamellar interfaces.

The reduced tensile ductility with respect to GE-SPS alloys is likely to be associated with the very high strength of TNB9-SPS alloys. During the present work, it was difficult to control the sample microstructures and, the room temperature tensile tests and creep experiments showed no clear dependence on the sintering conditions. In the author's opinion, these difficulties result from the very high sensitivity of the microstructure formed during SPS on small deviations in chemical composition. This sensitivity is enhanced by the retention of the dendritic morphology of the powder. Such an effect is related to the solidification pathway upon cooling during gas atomisation of the powders and appears to influence the microstructure during all subsequent processing stages. For a better understanding, it will be necessary to perform accurate and statistical microstructural analyses of undeformed and deformed samples by SEM and TEM. Attempts to homogenize the microstructures will also

be made by using longer holding times at plateau temperature during the SPS experiments. Alternatively one could investigate the influence of different powder size fractions, as segregation is reduced in smaller particles.

## **8. Conclusion**

In the present work, a Ti-46Al-9Nb powder was successfully sintered by Spark Plasma Sintering. Powder compacts of 8 and 36 mm diameter were sintered at temperatures ranging between 1250°C and 1300°C. Depending on the sintering temperature, two-phased, duplex and lamellar microstructures were obtained, as would be expected from the corresponding phase diagram [25]. A quasi- $\alpha_2$  phase was found at the lowest sintering temperatures in a two-phased microstructure, which is in fact an  $\alpha_2$  phase in which Nb atoms have partly substituted Ti atoms. This phase is observed in both a lath microstructure and as small grains between the larger  $\gamma$  grains.

Besides two specimens which failed prematurely during tensile tests due to the presence of some Fe inclusions, the TNB9-SPS materials exhibited high strength levels but a limited tensile ductility of less than 1% at room temperature. The mechanical properties show some scatter even for nominally identical sintering conditions and similar microstructures. The creep properties of TNB9-SPS are improved with respect to SPS alloys made from GE and G4 powders, but also show degree of scatter.

Microstructural control during SPS experiments using TNB powders was found to be difficult compared to GE and G4 powders [19,33]. This is due to local compositional variations in the powder particles and the associated sensitivity of high temperature transformation processes in the TNB alloys. This is especially severe for the duplex microstructures which only occur in a very narrow temperature range. Moreover, the retention of the dendritic morphology and the associated chemical inhomogeneities lead to extended microstructural heterogeneities that can affect the overall mechanical behaviour of TNB-SPS materials.

## **Acknowledgments**

The authors are thankful for the SPS facilities at the PNF2 (Plateforme Nationale de Frittage Flash/CNRS" in Toulouse, France).

This study was developed in the framework of the SPALSMAP project which is supported by the French regions Midi-Pyrénées and Aquitaine and by TURBOMECA (Groupe SNECMA) and LIEBHERR companies. All of them are strongly acknowledged.

The authors would like also to thank Stavos Nicolopoulos from Nanomegas for providing the electronic precession equipment and Jonathan Paul for reading of the manuscript.

## References

- [1] Chen G, Zhang W, Wang Y, Wang J, Sun Z. *Structural Intermetallics TMS*, 1993; 319.
- [2] Huang S, *Structural Intermetallics TMS*, 1993; 299.
- [3] Appel F, Oehring M., *Gamma-Titanium Aluminide Alloys: Alloy Design and Properties*. In: Leyens, C.; Peters, M. (Eds.): *Titanium and Titanium Alloys*, Wiley-VCH (2003) 89-152.
- [4] Liu ZC, Lin JP, Li SJ, Chen GL. *Intermetallics* 2002; 10: 653.
- [5] Zhang WJ, Deevi SC, Chen GL., *Intermetallics* 2002; 10: 403.
- [6] Paul JDH, Appel F, Wagner R., *Acta Mater.* 1998; 46: 1075.
- [7] Appel F, Paul JDH, Oehring M, Fröbel U, Lorenz U. *Metallurgical and materials Transactions A* 2003; 34A: 2149.
- [8] Gebhard S, Pyczak F, Göken M *Materials Science and Engineering A* 2009; 523: 235.
- [9] Paul JDH, Oehring M, Hoppe R, Appel F. *Gamma Titanium Aluminides*, TMS 2003; 403.
- [10] Cheng TT, Willis MR, Jones IP. *Intermetallics* 1999;7: 89.
- [11] Bystrzanowski S, Bartels A, Clemens H, Gerling R, Schimansky FP, Dehm G, Kestler H. *Intermetallics* 2005; 13: 515.
- [12] Bystrzanowski S, Bartels A, Clemens H, Gerling R, Schimansky FP, Dehm G. *Mater Res. Soc. Symp. Proc.* 2005 ; S7.12.1.
- [13] Bystrzanowski S, Bartels A, Clemens H, Gerling R. *Intermetallics* 2008; 16: 717.
- [14] Orru R, Licheri R, Mario Locci A, Cincotti A, Cao G. *Materials Science and Engineering* 2009; R63:127.
- [15] Calderon HA, Garibay-Febles V, Umemoto M, Yamaguchi M, *Materials Science and Engineering A* 2002; 329-331: 196.
- [16] Chen YY, Yu HB, Zhang DL, Chai LH, *MSEA, Materials Science and Engineering A* 2009; 525: 166.
- [17] Xiao S, Tian J, Xu L, Chen Y, Yu H, Han J. *Trans. Nonferrous Met. Soc. China* 2009; 19:1423.
- [18] Molénat G, Thomas M, Galy J, Couret A. *Advanced Engineering Materials* 2007; 9-8: 667.
- [19] Couret A, Molénat G, Galy J, Thomas M. *Intermetallics* 2008; 16: 1134.
- [20] Wang YH, Lin JP, He YH, Wang YL, Chen GL. *Intermetallics* 2008; 16: 215.
- [21] Wang YH, Lin JP, He YH, Wang YL, Chen GL. *Materials Science and Engineering A* 2009; 489: 55.
- [22] Lu X, He XB, Zhang B, Zhang L, Qu XH, Guo ZX. *Intermetallics* 2009; 17: 840.
- [23] Gerling R, Clemens H, Schimansky FP. *Advanced Engineering Materials* 2004; 6: 23.
- [24] Gerling R, Bartels A, Clemens H, Kestler H, Schimansky FP. *Intermetallics* 2004; 12: 275.
- [25] Chen GL, Xu XJ, Teng ZK, Wang YL, Lin JP. *Intermetallics* 2007; 15: 625.

- [26] Agote I, Coletto J, Gutiérrez M, Sargsyan A, García de Cortazar M, Lagos MA, Borovinskaya IP, Sytshev AE, Kvanin VL, Balikhina NT, Vadchenko SG, Lucas K, Wisbey A, Pambaguian L. *Intermetallics* 2008;16 : 1310.
- [27] Vincent R, Midgley PA. *Ultramicroscopy* 1994; 53: 271.
- [28] Houdellier F, Roucau C., Clement L, Rouviere JL, Casanove MJ. *Ultramicroscopy* 2006; 106: 951.
- [29] Appel F, Paul JDH, Oehring. *Materials Science and Engineering A* 2009; 510: 342.
- [30] Zghal S, Thomas M, Naka S, Finel A, Couret A, *Acta Mater.* 2005; 53: 2653.
- [31] Chladil HF, Clemens H, Leitner H, Bartels A, Gerling R, Schimansky FP, Kremmer S. *Intermetallics* 2006; 14: 1194.
- [32] Chladil HF, Clemens H, Takeyama M, Kozeschnick E, Bartels A, Gerling R, Kremmer S. *Mater Res. Soc. Symp. Proc.* 2007 ; 980: II07-03.
- [33] Jabbar H. Monchoux JP, Thomas M, Couret A. *Mater Res. Soc. Symp. Proc.* 2009 ; 1128: 103..
- [34] Picca FE, Véron M, Bréchet Y. *Matériaux & Techniques* 2004 ; 1-2 : 59.

## Figure caption

Fig. 1: X-ray diffraction spectra and SEM micrographs of the initial powder and of samples sintered at various temperatures.

- a) DRX spectra
- b)  $T_s = 975^\circ\text{C}$
- c)  $T_s = 1250^\circ\text{C}$
- d)  $T_s = 1275^\circ\text{C}$
- e)  $T_s = 1300^\circ\text{C}$

Fig. 2: TEM dark field images of three laths (a) and a grain (b) of the quasi- $\alpha_2$  phase.

Fig. 3: Electron diffraction patterns along the [0001] zone axis

- (a) experimental precession pattern
- (b) calculated pattern.

Fig. 4 : CBED patterns

- (a) and (b) out of zone axis at various locations
- (c) in [0001] zone axis

Fig. 5: HREM picture of the quasi- $\alpha_2$  phase in  $[\bar{2}201]$  zone axis

Fig. 6: SEM BSE (a & b) and TEM (c & d) images of the two-phased microstructure. A and B refer to different  $\gamma$  grains (see text for details). Some quasi- $\alpha_2$  grains and laths are indicated by arrows and some B2 precipitates are encircled. (c) is an enlargement of a A  $\gamma$  grain. (d) is an enlargement of the B zone.

Fig. 7: TEM micrographs of the duplex microstructure.

- (a) and (b) usual lamellar grain in a recrystallized area
- (c) and (d) lamellar grain formed at a temperature lower than the  $\alpha \rightarrow \alpha_2$  transformation temperature
- (e)  $\gamma$  grain crossed by laths.

Fig. 8: Tensile curves at room temperature of TNB9-SPS samples. For comparison, a curve obtained for a HIPed specimen from the same powder is also shown. The temperatures given are the sample temperatures during SPS densification.

Fig. 9: SEM fractography (a & b) of the sample that broke prematurely ( $T_s = 1260^\circ\text{C}$ ). 1, 2 and 3 indicate the points at which the chemical analyses reported in Table 4 were made.

Fig. 10: Tensile creep curves at 300MPa-700°C of TNB9-SPS samples. The temperatures given are the sample temperatures during SPS processing. The experiments were performed under constant stress.

## Table caption

Tab 1: Average compositions in at. % of dendrite cores and interdendritic channels. For these measurements, the error bars is about  $\pm 1\%$ .

Table 2: EDX point analysis of the three phases identified in the two-phased microstructure. For these measurements, the error bars is about  $\pm 1\%$ .

Table 3: Results of tensile tests at room temperature ( $T_s$  : sample temperature during the SPS densification, YS : Yield Stress, UTS : Ultimate Tensile Stress, A : plastic elongation at rupture). GI, GII and GIII refer to three different groups of samples define in the text.

Table 4: EDX analysis at the three points marked in Fig. 9b. For these measurements, the error bars is about  $\pm 1\%$ .

Table 5: Minimum creep rate ( $\dot{\epsilon}_{\min}$ ) at 700°C and 300 MPa ( $T_s$  sample temperature during the SPS densification).

	Ti	Al	Nb
Dendrite cores	44-47	41-45	10-12
Interdendritic channels	44-46	45-48	7-9

Table 1

	Al	Ti	Nb
$\gamma$	44	45	11
quasi- $\alpha_2$	39	50	11
B2	39	48	13

Table 2

$T_s$	UTS [MPa]	$Y_s$ [MPa]	A [%]	
1240	812	Early failure		} GI
1260	826	Early failure		
1250	821	774	0.88	} GII
1290	794	787	0.44	
1250	882	-	0.15	} GIII
1260	889	874	0.78	
1280	872	867	0.56	

Table 3

Element	Ti	Al	Nb	Cr	Fe
Point 1	52	41	7	0	0
Point 2	51	41	8	0	0
Point 3	62	4	0	3	31

Table 4

$T_s$ (°C)	$\dot{\varepsilon}_{\min}$ (s <sup>-1</sup> )
1240	$1 \cdot 10^{-7}$
1250	$8 \cdot 10^{-8}$
1250	$5 \cdot 10^{-8}$
1260	$6 \cdot 10^{-8}$

Table 5

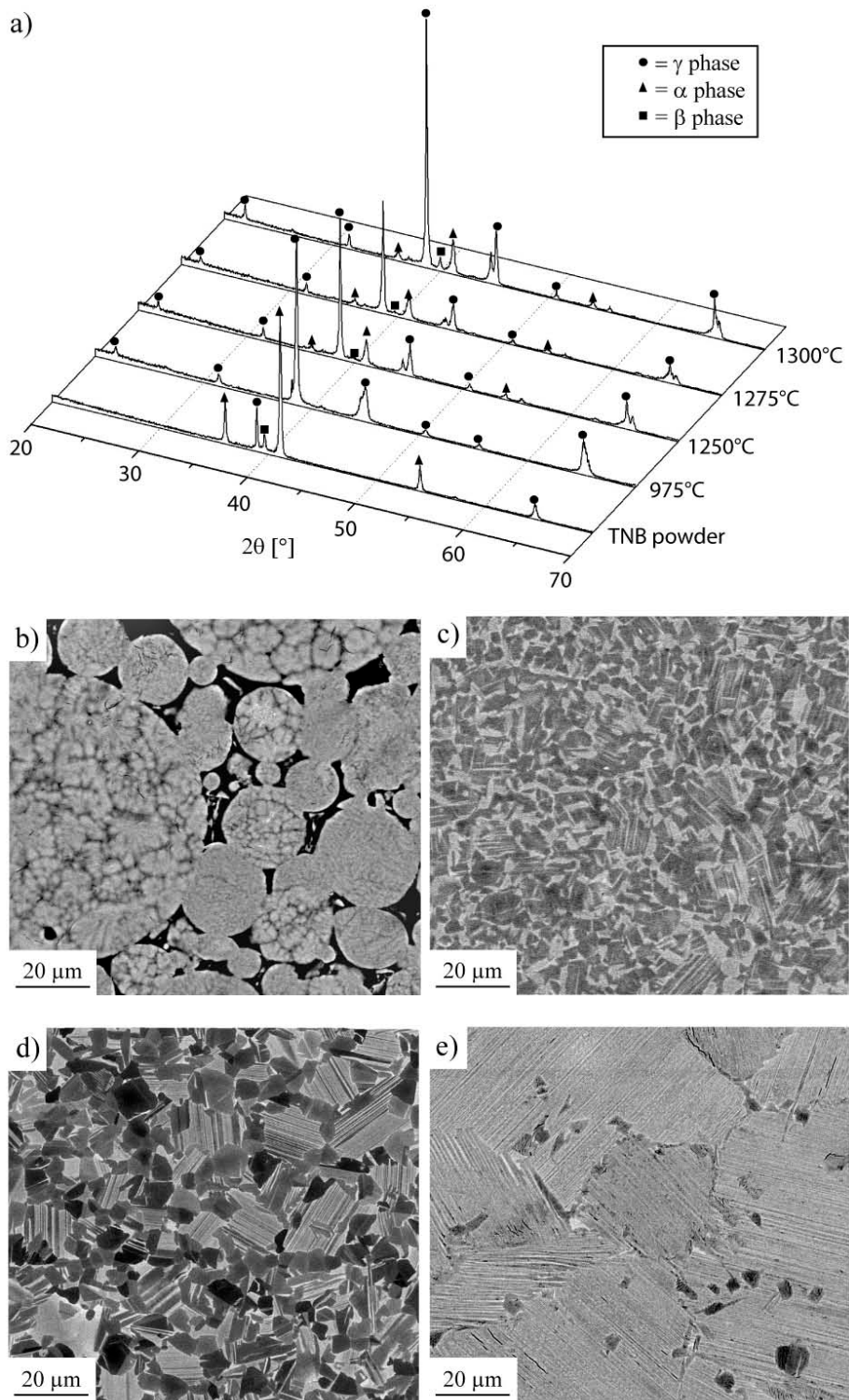


Fig. 1

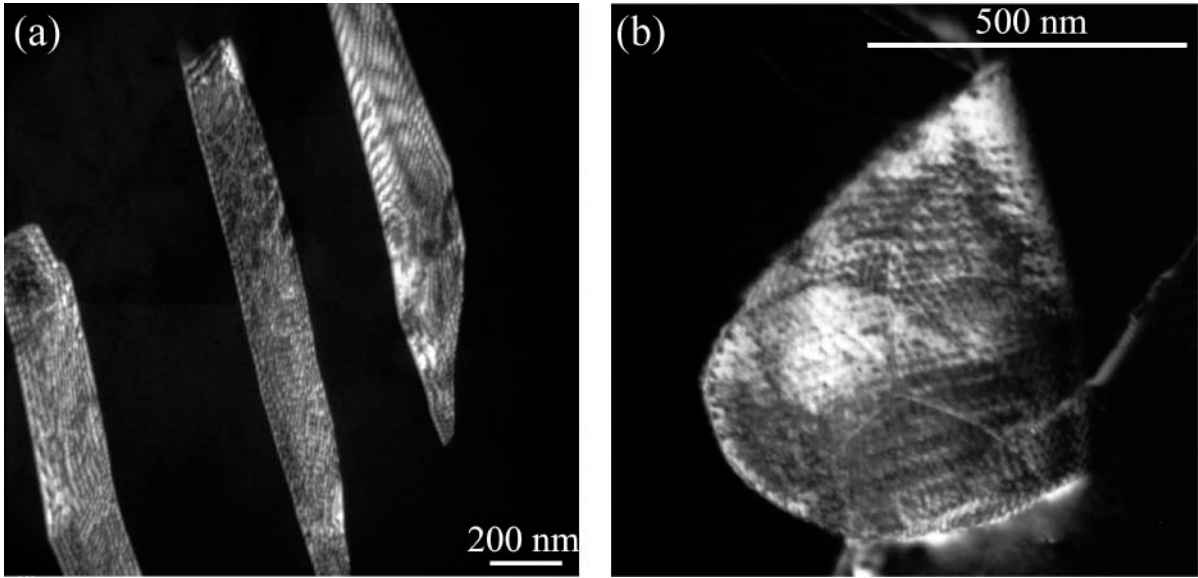


Fig. 2

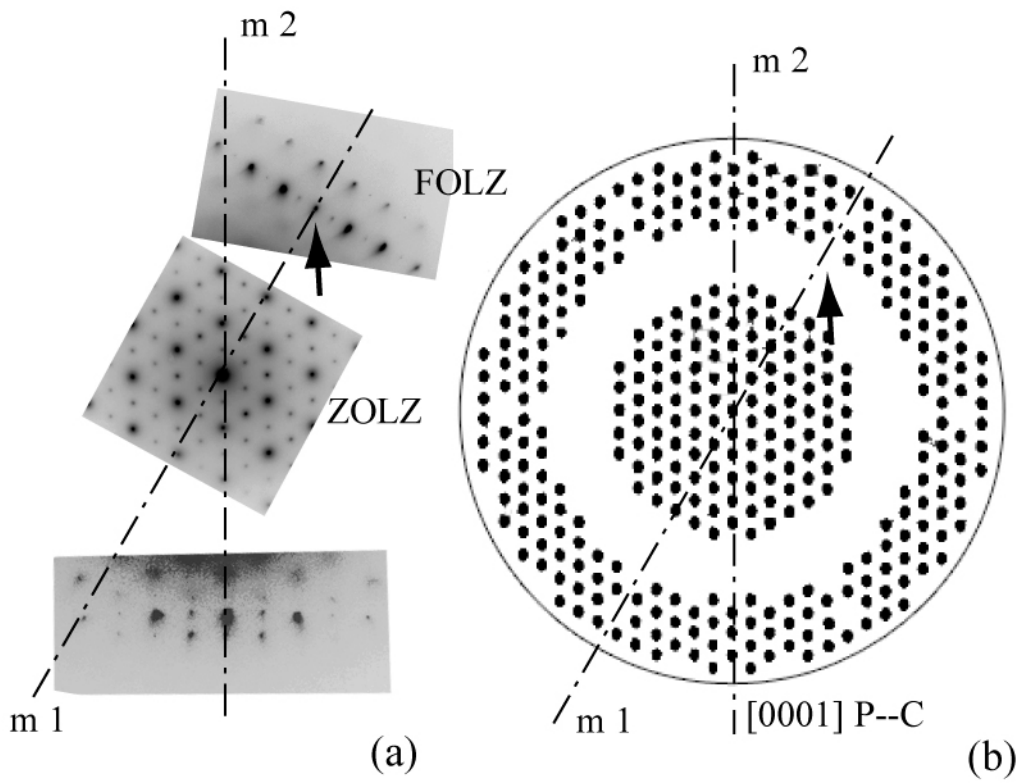


Fig. 3

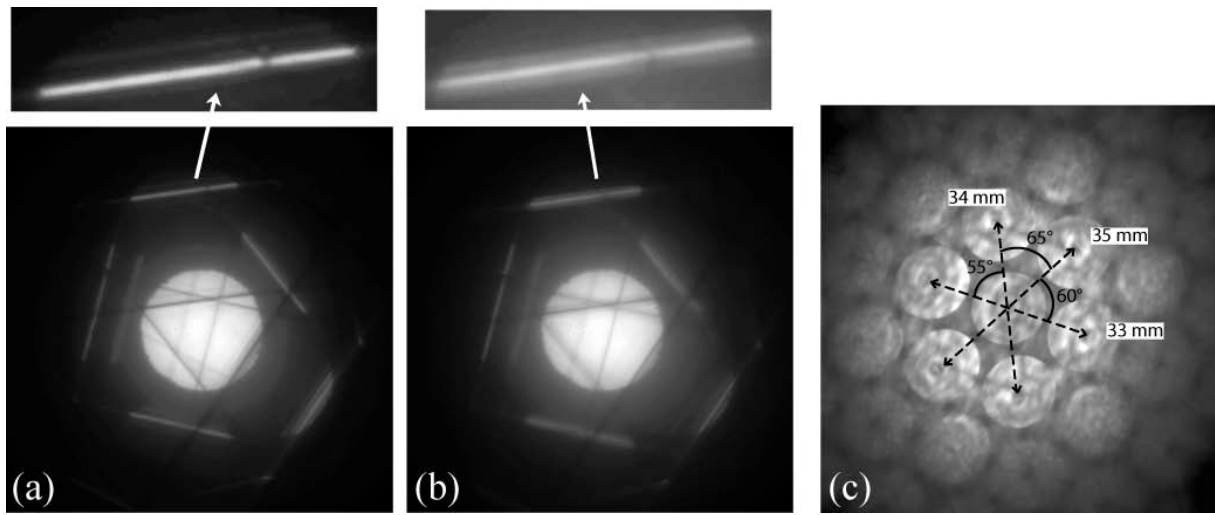


Fig. 4

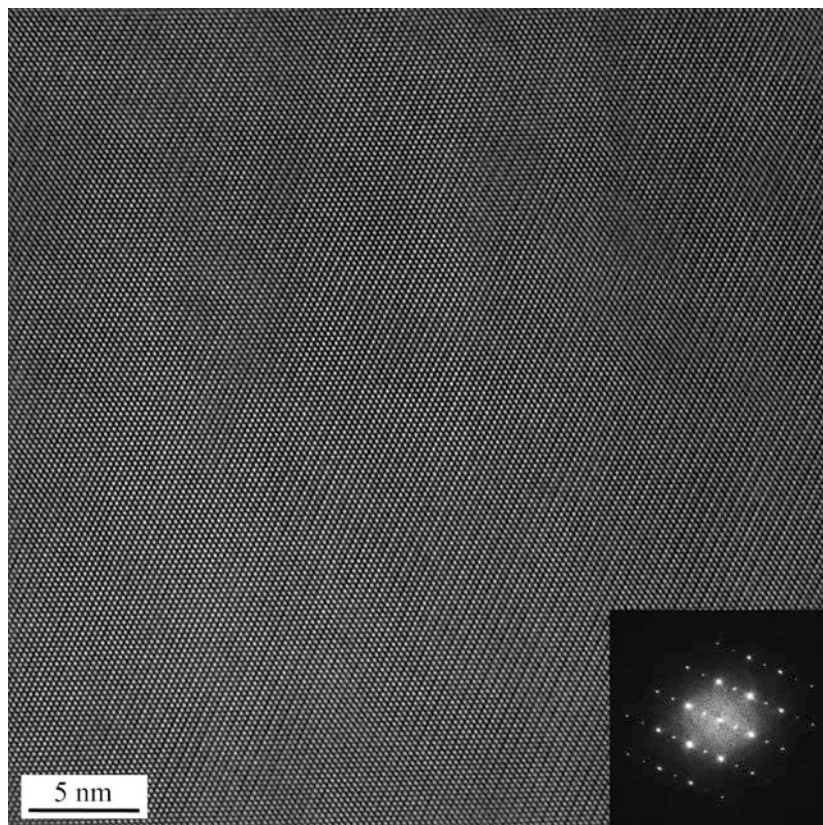


Fig.5



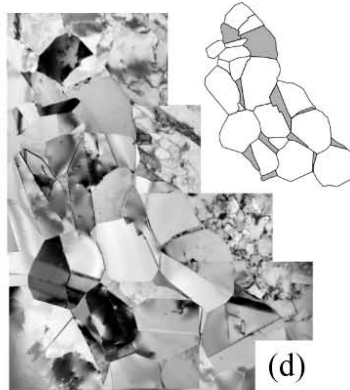
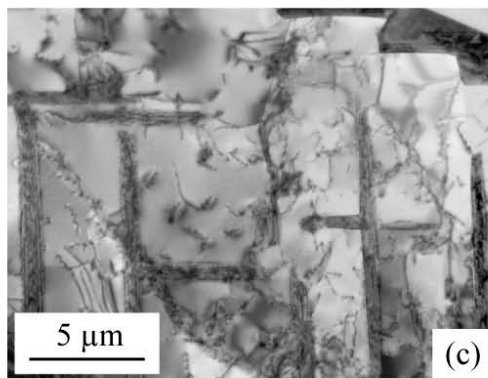
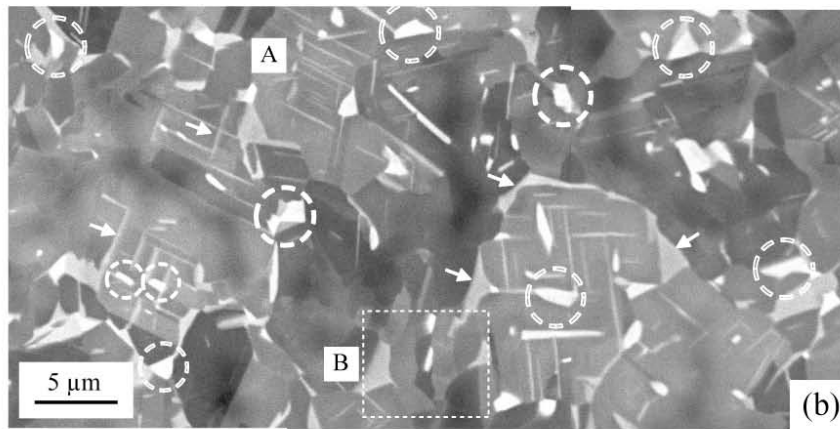
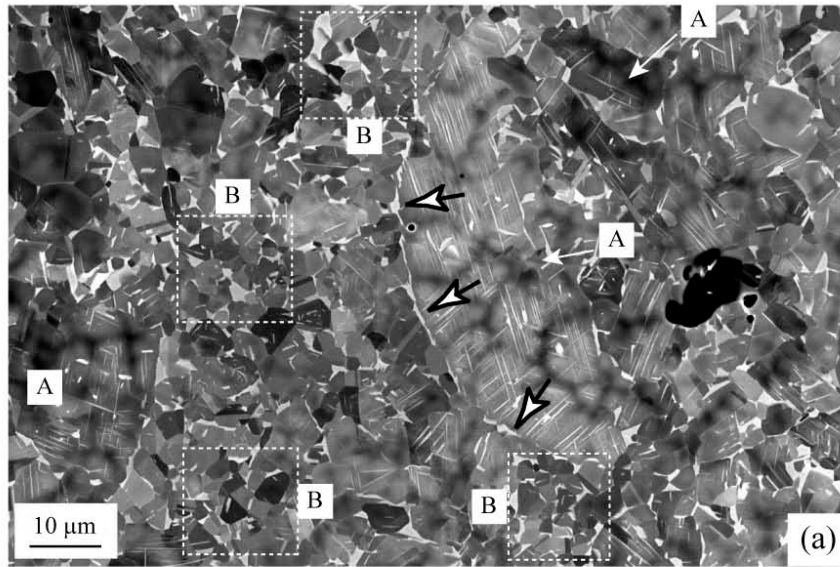


Fig. 6

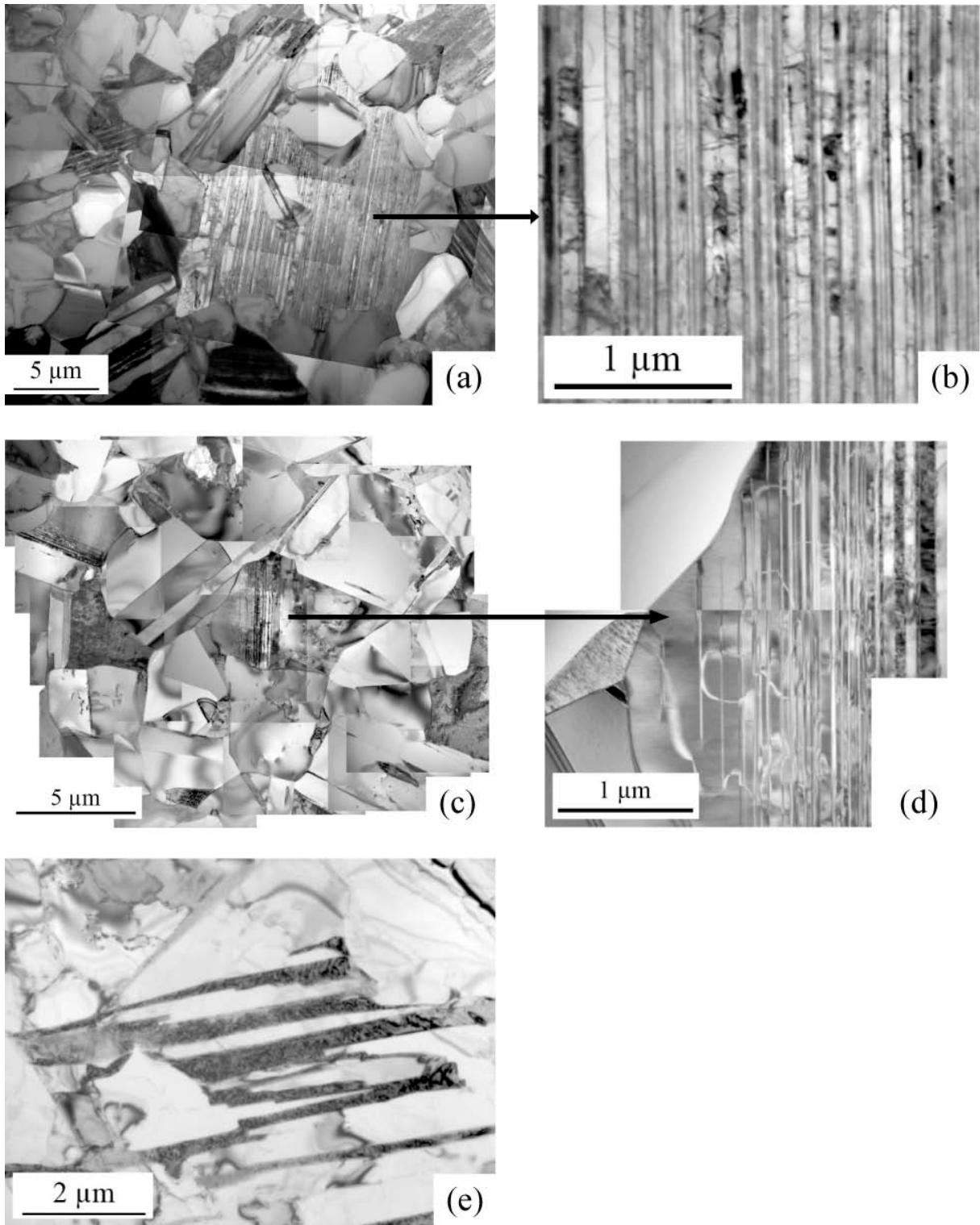


Fig. 7

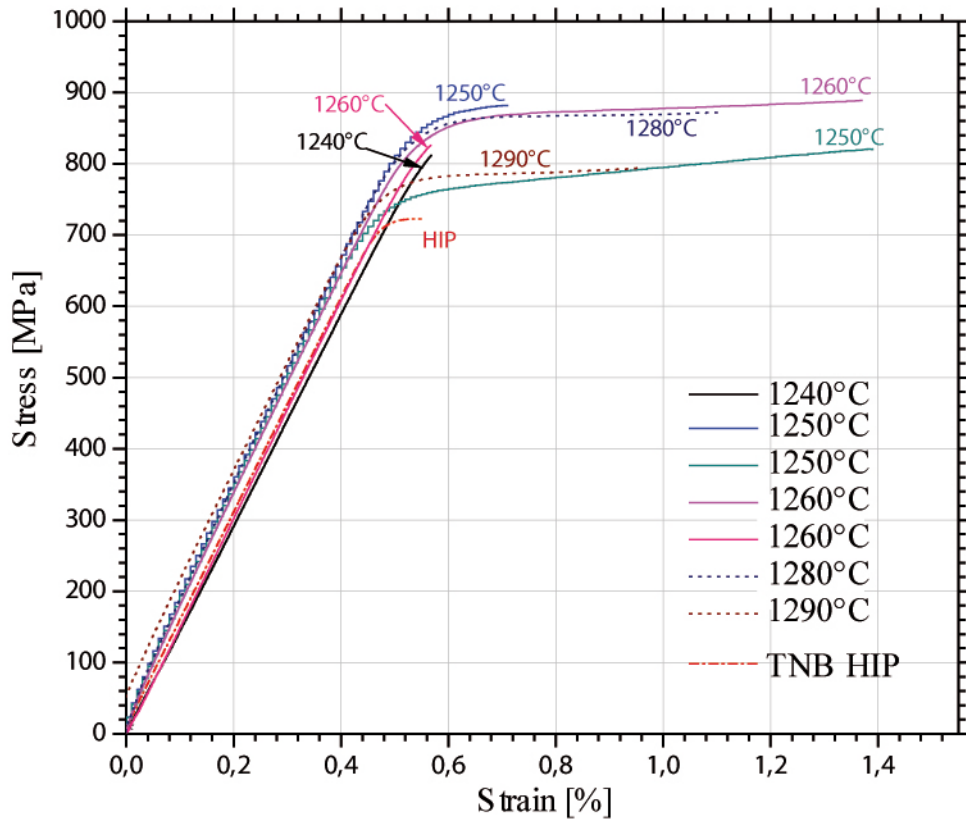


Fig. 8

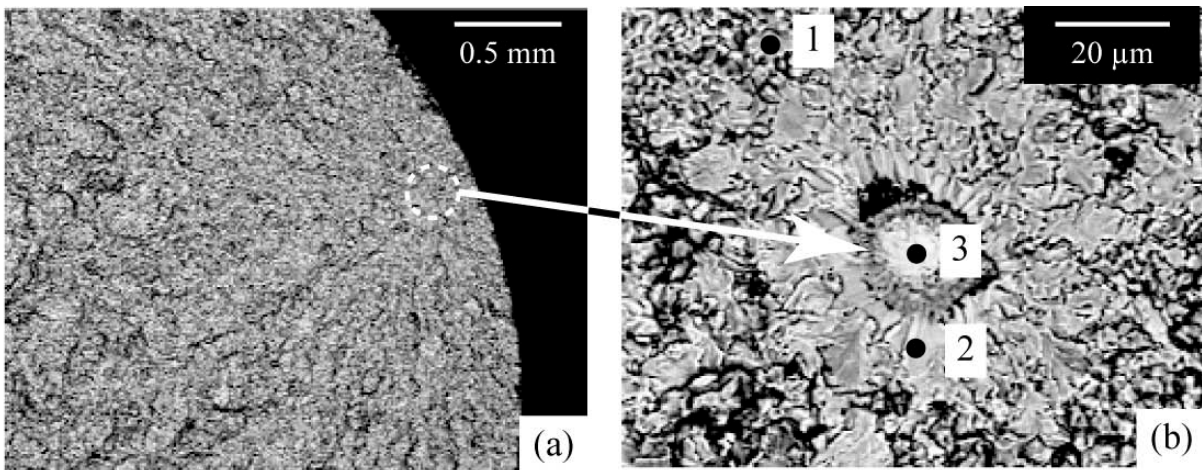


Fig. 9

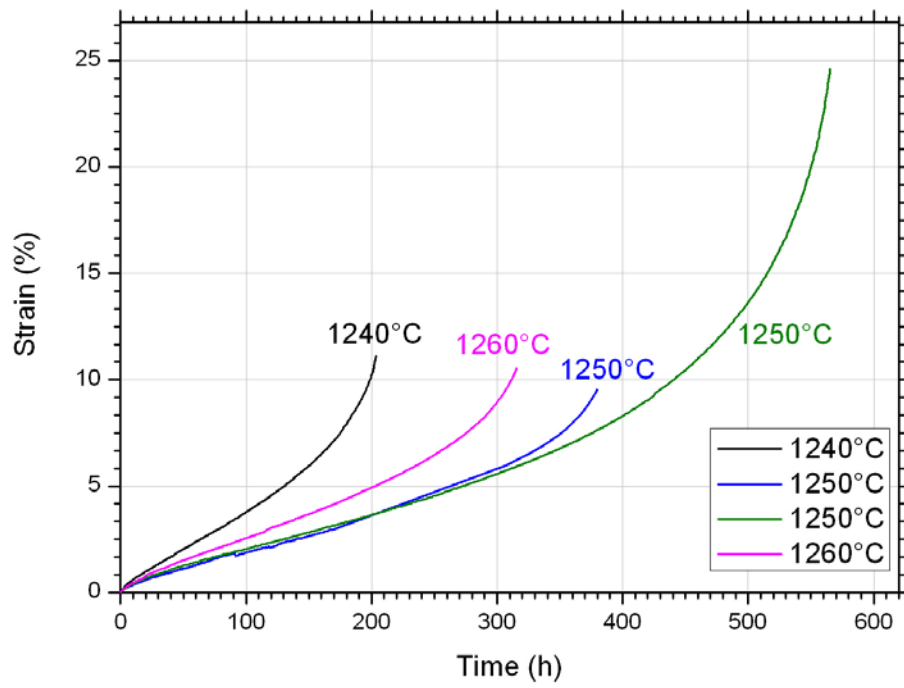


Fig. 10